

# Nonlinear bayesian tomography of ion temperature and velocity for Doppler coherence imaging spectroscopy in RT-1

Kenji. Ueda<sup>1, a)</sup> and Masaki. Nishiura<sup>1,2</sup>

<sup>1)</sup>National Institute of Fusion Science

<sup>2)</sup>University of Tokyo

(Dated: 17 October 2024)

We present a novel Bayesian tomography approach for Coherence Imaging Spectroscopy (CIS) that simultaneously reconstructs ion temperature and velocity distributions in plasmas. Utilizing nonlinear Gaussian Process Tomography (GPT) with the Laplace approximation, we model prior distributions of log-emissivity, temperature, and velocity as Gaussian processes. This framework rigorously incorporates nonlinear effects and temperature dependencies often neglected in conventional CIS tomography, enabling robust reconstruction even in the region of high temperature and velocity. By applying a log-Gaussian process, we also address issues like velocity divergence in low-emissivity regions. Validated with phantom simulations and experimental data from the RT-1 device, our method reveals detailed spatial structures of ion temperature and toroidal ion flow characteristic of magnetospheric plasma. This work significantly broadens the scope of CIS tomography, offering a robust tool for plasma diagnostics and facilitating integration with complementary measurement techniques.

## I. INTRODUCTION

Magnetospheric plasmas are fundamental plasma systems capable of producing high-beta environments with diverse confinement structures<sup>1,2</sup>. Understanding the spatial distributions of ion temperature and toroidal flow velocity in such plasmas is crucial for advancing our knowledge of confinement and transport phenomena. The Ring Trap-1 (RT-1) device confines high-beta plasma by generating a dipole magnetic field through the levitation of a superconducting toroidal coil<sup>3,4</sup>. In this device, fast toroidal flows correlated with ion temperature have been observed<sup>5</sup>. In contrast to tokamaks and stellarators, where plasma parameters on closed magnetic surfaces in the core region are often considered to be constant, the dipole magnetic field in RT-1 leads to spatially non-uniform plasma parameters due to mirror effects caused by inhomogeneities in the magnetic field strength.

To achieve comprehensive measurements of magnetospheric plasmas in RT-1, coherence imaging spectroscopy (CIS) has been introduced<sup>6,7</sup>. CIS is a relatively new diagnostic technique that enables two-dimensional imaging of ion temperature and velocity through the Doppler effect<sup>8-11</sup>. It has been successfully implemented in various devices, including DIII-D<sup>12,13</sup>, MAST<sup>14</sup>, W7-X<sup>15,16</sup>, and HL-2A<sup>17</sup>, particularly for imaging impurity flows in the scrape-off layer (SOL) region using CIII emission lines.

CIS only provides line-integrated projection images along the line of sight (LOS); therefore, tomographic techniques are required to reconstruct the local distribution of plasma parameters from these projections. Assuming axisymmetry, it is theoretically possible to reconstruct poloidal cross-sectional distributions from a single image. Tomography for CIS has been studied and implemented on several devices<sup>13,14,18-21</sup>. However, conventional tomography methods face several challenges and limitations:

- Linearization approximations: To solve the integral equations linearly, approximations are made regarding the velocity and temperature, which may not be valid in regions with significant flow.
- Handling zero emissivity: Difficulties of reconstructing the velocity arises when the emissivity becomes around zero, as dividing by zero leads to numerical issues.
- Neglect of temperature effects: The impact of ion temperature, manifesting as Doppler broadening, is often neglected, despite the fact that temperature and velocity are intricately intertwined in the process of line integration.

These limitations impose constraints on the design of CIS diagnostics and restrict the plasma conditions under which reliable tomography can be performed.

To overcome these challenges, we propose a comprehensive tomographic framework using Bayesian estimation to simultaneously reconstruct emissivity, ion temperature, and velocity. By applying nonlinear Gaussian Process Tomography (nonlinear GPT)<sup>22</sup> with Laplace approximation to CIS diagnostics, we aim to calculate reliable posterior probabilities of these parameters while satisfying the exact integral equations without relying on linear approximations.

In this paper, we first describe the basic concepts of tomography and introduce nonlinear GPT in Section II. Section III explains the measurement principles of CIS and organizes the essential equations for tomography. In Section IV, we develop the Bayesian model for deriving the posterior probabilities of ion temperature and velocity in CIS. Section V validates the proposed method using phantom data, with RT-1 as a case study. Finally, Section VI presents the results using experimental data from RT-1, demonstrating the effectiveness of the proposed method.

<sup>a)</sup>Electronic mail: ueda.kenji@nifs.ac.jp

## II. GAUSSIAN PROCESS TOMOGRAPHY

### A. Bayesian Tomography Using Gaussian Processes

In plasma diagnostics, one of the primary objectives is to reconstruct an unknown local quantity  $f(\vec{r})$ , such as emissivity, temperature, or velocity, from observed data  $d(\vec{x})$ , where  $\vec{r}$  represents positions within the plasma, and  $\vec{x}$  denotes sensor coordinates. Bayesian tomography provides a systematic framework for this inverse problem by incorporating prior knowledge and observed data to estimate the posterior probability of the unknown quantity. According to Bayes' theorem, the posterior probability of  $f$  given the data  $d$  and hyperparameters  $\theta$  is expressed as:

$$\begin{aligned} \underbrace{p(f | d, \theta)}_{\text{posterior}} &= \frac{\underbrace{p(d | f, \theta)}_{\text{likelihood}} \underbrace{p(f | \theta)}_{\text{prior}}}{\underbrace{p(d | \theta)}_{\text{evidence}}}, \\ &\propto p(d | f, \theta) \times p(f | \theta). \end{aligned} \quad (1)$$

In Gaussian Process Tomography (GPT)<sup>23–25</sup>, the prior probability  $p(f | \theta)$  is modeled as a Gaussian process. This implies that any finite collection of function values  $\mathbf{f} = \{f(\vec{r}_i)\}_{i=1}^N$  follows a multivariate normal distribution characterized by a mean vector  $\boldsymbol{\mu}_f$  and a covariance matrix  $K_f$ :

$$\begin{aligned} p(\mathbf{f} | \theta) &= \mathcal{N}(\mathbf{f} | \boldsymbol{\mu}_f, K_f) \\ &= \frac{1}{(2\pi)^{N/2} |K_f|^{1/2}} \exp\left(-\frac{1}{2}(\mathbf{f} - \boldsymbol{\mu}_f)^T K_f^{-1} (\mathbf{f} - \boldsymbol{\mu}_f)\right), \end{aligned}$$

where  $\mathcal{N}$  denotes the normal distribution,  $N$  is the number of discretized points in the plasma domain, and  $|K_f|$  is the determinant of the covariance matrix. The covariance matrix  $K_f$  is constructed using a kernel function  $k(\vec{r}_i, \vec{r}_j)$ , such that  $\{K_f\}_{i,j} = k(\vec{r}_i, \vec{r}_j)$ .

The choice of kernel function  $k(\cdot, \cdot)$  is crucial, as it encodes our assumptions about the smoothness and spatial correlations of the unknown function  $f(\vec{r})$ . In this paper, we employ the Gibbs kernel<sup>24,26</sup>, a generalization of the squared exponential (SE) kernel, defined as:

$$\begin{aligned} k(\vec{r}_i, \vec{r}_j) &= \sigma_f^2 |\Sigma_\ell(\vec{r}_i)|^{\frac{1}{4}} |\Sigma_\ell(\vec{r}_j)|^{\frac{1}{4}} \left| \frac{\Sigma_\ell(\vec{r}_i) + \Sigma_\ell(\vec{r}_j)}{2} \right|^{-\frac{1}{2}} \\ &\times \exp\left(-\frac{1}{2}(\vec{r}_i - \vec{r}_j)^T \left(\frac{\Sigma_\ell(\vec{r}_i) + \Sigma_\ell(\vec{r}_j)}{2}\right)^{-1} (\vec{r}_i - \vec{r}_j)\right), \end{aligned} \quad (2)$$

where  $\sigma_f^2$  represents the signal variance, and  $\Sigma_\ell(\vec{r})$  is a generalized scaling matrix defining the length scales of the process at location  $\vec{r}$ , which is related to the inverse matrix of the metric tensor. When  $\Sigma_\ell(\vec{r})$  is a scalar multiple of the identity matrix,  $\Sigma_\ell(\vec{r}) = \ell^2 I$ , the Gibbs kernel reduces to the standard SE kernel commonly used in Gaussian processes:

$$k(\vec{r}_i, \vec{r}_j) = \sigma_f^2 \exp\left(-\frac{|\vec{r}_i - \vec{r}_j|^2}{2\ell^2}\right).$$

However, in this study, we consider isotropic but non-uniform kernels to accommodate spatially varying correlation lengths within the plasma. Accordingly, the scaling matrix  $\Sigma_\ell(\vec{r})$  is defined as:

$$\Sigma_\ell(\vec{r}) = \ell^2(\vec{r}) I = \begin{bmatrix} \ell^2(\vec{r}) & 0 \\ 0 & \ell^2(\vec{r}) \end{bmatrix}, \quad (3)$$

where  $\ell(\vec{r})$  is the position-dependent length scale function, and  $I$  is the identity matrix. This formulation allows the kernel to adapt to local variations in the plasma, providing more flexibility in modeling spatial correlations.

### B. Nonlinear Gaussian Process Tomography

In practical applications, the relationship between the observed data  $d$  and the unknown local quantity  $f$  is not always linear. Therefore, we consider the following general measurement model:

$$\mathbf{d} = \mathbf{g}(\mathbf{f}) + \boldsymbol{\epsilon}, \quad (4)$$

where  $\mathbf{g}(\mathbf{f})$  is a nonlinear function mapping the local quantity  $\mathbf{f} = \{f(\vec{r}_i)\}_{i=1}^N$  to the observed data  $\mathbf{d} = \{d(\vec{x}_i)\}_{i=1}^M$ , and  $\boldsymbol{\epsilon}$  represents the measurement error, including random noise and systematic errors, assumed to be normally distributed with zero mean and covariance  $\Sigma_g$ .

Assuming the prior probability of  $\mathbf{f}$  is Gaussian with mean  $\boldsymbol{\mu}_f^{\text{pri}}$  and covariance  $K_f$ , and the noise  $\boldsymbol{\epsilon}$  follows a Gaussian distribution with covariance  $\Sigma_g$ , the posterior probability of  $\mathbf{f}$  given the data  $\mathbf{d}$  can be expressed as:

$$\begin{aligned} \underbrace{\log p(\mathbf{f} | \mathbf{d}, \theta)}_{\text{log-posterior}} &= \underbrace{-\frac{1}{2}(\mathbf{d} - \mathbf{g}(\mathbf{f}))^T \Sigma_g^{-1} (\mathbf{d} - \mathbf{g}(\mathbf{f}))}_{\text{log-likelihood}} \\ &\quad - \underbrace{\frac{1}{2}(\mathbf{f} - \boldsymbol{\mu}_f^{\text{pri}})^T K_f^{-1} (\mathbf{f} - \boldsymbol{\mu}_f^{\text{pri}})}_{\text{log-prior}} + C, \end{aligned} \quad (5)$$

where  $C$  is a constant independent of  $\mathbf{f}$ . The first term represents the log-likelihood, and the second term is the log-prior.

In the case where  $\mathbf{g}(\cdot)$  is a linear operator, the posterior distribution remains Gaussian, and analytical solutions are available, as seen in the standard GPT<sup>23–25</sup>. However, when  $\mathbf{g}(\cdot)$  is nonlinear, as in many practical situations, the posterior probability becomes non-Gaussian, and obtaining an analytical solution is intractable because Eq. (5) is no longer a quadratic form in  $\mathbf{f}$ .

To address this challenge, we employ the Laplace approximation<sup>27,28</sup>, which approximates the posterior probability by a Gaussian centered at the mode of the true posterior. Specifically, we denote:

$$p(\mathbf{f} | \mathbf{d}, \theta) \stackrel{\text{LA}}{\simeq} \mathcal{N}(\mathbf{f} | \tilde{\boldsymbol{\mu}}^{\text{LA}}, \tilde{\Sigma}^{\text{LA}}), \quad (6)$$

where  $\tilde{\boldsymbol{\mu}}^{\text{LA}}$  is the mode of the posterior distribution, and  $\tilde{\Sigma}^{\text{LA}}$  is the inverse of the negative Hessian (second derivative) of the

log-posterior evaluated at the mode. Mathematically, these are defined as:

$$\tilde{\boldsymbol{\mu}}^{\text{LA}} = \underset{\boldsymbol{f}}{\text{arg max}} \Psi(\boldsymbol{f}), \quad (7)$$

$$\tilde{\boldsymbol{\Sigma}}^{\text{LA}} = - \left[ \nabla^2 \Psi(\boldsymbol{f}) \Big|_{\boldsymbol{f}=\tilde{\boldsymbol{\mu}}^{\text{LA}}} \right]^{-1}, \quad (8)$$

where  $\Psi(\boldsymbol{f})$  is the unnormalized log-posterior function, given by  $\Psi(\boldsymbol{f}) \stackrel{\text{const}}{=} \log p(\boldsymbol{f} | \boldsymbol{d}, \boldsymbol{\theta})$ . To find the mode  $\tilde{\boldsymbol{\mu}}^{\text{LA}}$ , we solve the optimization problem in Eq. (7). This can be achieved using iterative methods such as the Newton-Raphson algorithm. The update rule for the Newton-Raphson method is given by:

$$\tilde{\boldsymbol{f}}^{\text{new}} = \tilde{\boldsymbol{f}}^{\text{old}} - \alpha \left[ \nabla^2 \Psi(\tilde{\boldsymbol{f}}^{\text{old}}) \right]^{-1} \nabla \Psi(\tilde{\boldsymbol{f}}^{\text{old}}), \quad (9)$$

where  $\tilde{\boldsymbol{f}}^{\text{old}}$  is the current estimate,  $\tilde{\boldsymbol{f}}^{\text{new}}$  is the updated estimate,  $\nabla \Psi(\tilde{\boldsymbol{f}}^{\text{old}})$  is the gradient of the log-posterior,  $\nabla^2 \Psi(\tilde{\boldsymbol{f}}^{\text{old}})$  is the Hessian matrix, and  $\alpha$  is a step size parameter. This iterative process is repeated until convergence, which is typically assessed when the norm of the gradient  $\|\nabla \Psi(\tilde{\boldsymbol{f}}^{\text{new}})\|$  becomes sufficiently small, indicating that a local maximum has been found. The step size  $\alpha$  can be set to 1 for simplicity, but choosing an optimal  $\alpha$  at each iteration can enhance convergence. Once the mode  $\tilde{\boldsymbol{\mu}}^{\text{LA}}$  is obtained, the covariance  $\tilde{\boldsymbol{\Sigma}}^{\text{LA}}$  is computed using Eq. (8). This provides an approximate Gaussian posterior distribution.

### III. DIAGNOSTICS WITH COHERENCE IMAGING SPECTROSCOPY

#### A. Measurement Principle

Coherence Imaging Spectroscopy (CIS) is a relatively new diagnostic method that realizes Doppler spectroscopy as an imaging technique, enabling two-dimensional measurement of ion temperature and velocity. It produces fringe images by exploiting the interference patterns created due to phase differences introduced by birefringent crystals. The signal from the output image of CIS,  $S_{\text{CIS}}(\vec{x})$ , is expressed as follows:

$$S_{\text{CIS}}(\vec{x}) = I_0 + I_0 \zeta_{\text{I}} \zeta_{\text{D}} \cos(\phi_0 + \phi_{\text{D}}) + \varepsilon. \quad (10)$$

It should be noted that each variable on the *right-hand side* of Eq. (10) is a function of  $\vec{x}$ , but this dependence has been omitted for simplicity. In this equation, the first term, denoted as  $I_0$ , represents the bias component corresponding to the intensity of the incident light. The second term is the modulation component corresponding to the autocorrelation of the incident light and depends on  $I_0$ ,  $\zeta_{\text{I}}$ ,  $\zeta_{\text{D}}$ ,  $\phi_0$ , and  $\phi_{\text{D}}$ . Among these, the instrumental contrast and phase of the carrier fringe,  $\zeta_{\text{I}}$  and  $\phi_0$ , respectively, must be eliminated from the data by a suitable calibration technique. The contrast factor, represented by the variable  $\zeta_{\text{D}}$ , is mainly affected by Doppler broadening of the spectrum, while the phase shift, represented by the variable  $\phi_{\text{D}}$ , is mainly affected by the Doppler shift.

#### B. Projection Equation

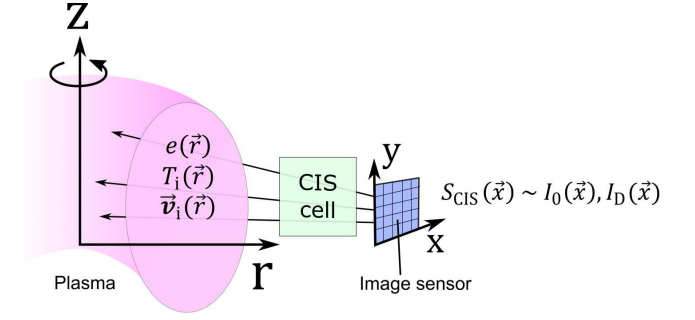


FIG. 1. Conceptual illustration of the relationship between local variables and observations in CIS.  $e(\vec{r})$ ,  $T_i(\vec{r})$ , and  $\vec{v}_i(\vec{r})$  are local emissivity, local ion temperature, and local ion flow velocity, respectively.  $S_{\text{CIS}}(\vec{x})$  is the observed image measured with CIS.  $\vec{r}$  is the coordinate in the plasma region, and  $\vec{x}$  is the coordinate on the image sensor.

The signal measured with CIS is the result of line integration of physical quantities including the emissivity  $e$ , ion temperature  $T_i$ , and ion velocity  $\vec{v}_i$  in the plasma, as shown in Fig. 1. Assuming that ions in the plasma are distributed according to a Maxwellian distribution and emit radiation with a singlet line such as the 468 nm line of He II, the relationship between the measured data,  $S_{\text{CIS}}(\vec{x})$ , and the local variables  $T_i(\vec{r})$ ,  $\vec{v}_i(\vec{r})$ , and  $e(\vec{r})$  can be strictly derived (see Appendix A) as:

$$I_0(\vec{x}) = \int_{L(\vec{x})} e(\vec{r}) dl, \quad (11)$$

$$I_{\text{D}}(\vec{x}) = \int_{L(\vec{x})} e(\vec{r}) \exp[-\hat{T}(\vec{r})] \exp[i\hat{v}(\vec{r}) \cdot \hat{l}] dl, \quad (12)$$

where  $L(\vec{x})$  denotes the line of sight corresponding to the pixel at  $\vec{x}$ , and  $dl$  is the differential path length along  $L(\vec{x})$ . The left-hand sides correspond to the observed data acquired from Eq. (10), whereas the right-hand sides detail the line integrations performed along the LOS.  $I_{\text{D}}$  is the effective amplitude of the modulated component of  $S_{\text{CIS}}$ , which is given by:

$$I_{\text{D}}(\vec{x}) = I_0(\vec{x}) \zeta_{\text{D}}(\vec{x}) \exp[i\phi_{\text{D}}(\vec{x})]. \quad (13)$$

In this paper, the hat symbol  $\hat{\cdot}$  denotes dimensionless quantities;  $\hat{T}$  and  $\hat{v}$  are normalized as  $\hat{T} := T_i/T_c$  and  $\hat{v} := \vec{v}_i/v_c$ , respectively. Here,  $T_c$  and  $v_c$  are the characteristic temperature and characteristic velocity, given by:

$$k_{\text{B}} T_c = 2m_s v_c^2, \quad v_c = \frac{c}{2\pi \hat{N}(\vec{x})}, \quad (14)$$

where  $k_{\text{B}}$  is the Boltzmann constant,  $c$  is the speed of light,  $m_s$  is the mass of the ion species, and  $\hat{N}(\vec{x})$  is group delay, defined as

$$2\pi \hat{N} := -\lambda_0 \left. \frac{d\phi}{d\lambda} \right|_{\lambda=\lambda_0}, \quad (15)$$

where  $\lambda_0$  is the central wavelength of the spectrum. The first equation, Eq. (11), is a standard projection equation, while the

second equation, Eq. (12), is a complex nonlinear equation where the emissivity, temperature, and velocity variables are intertwined, as discussed in the introduction.

### C. Organizing Equations for the Tomography

To simplify the solution of Eqs. (11) and (12), we introduce new variables  $\hat{e}$  and  $\hat{a}$ , defined as:

$$\hat{e} := \log e, \quad (16)$$

$$\hat{a} := \hat{e} - \hat{T}, \quad (17)$$

where we define  $\hat{e}$  and  $\hat{a}$  as the "log-emissivity" and the "local amplitude," respectively. By taking the logarithm of the emissivity, we combine the temperature and emissivity into a single variable,  $\hat{a}$ . Furthermore, previous studies<sup>22</sup> have indicated that this approach improves the accuracy of tomography.

Thus, Eqs. (11) and (12) can be rewritten and discretized for each  $i$  as follows:

$$\{g_0(\hat{e})\}_i := \sum_{j=1}^N H_{ij} \exp \hat{e}_j, \quad (18)$$

$$\{g_C(\hat{a}, \hat{v})\}_i := \sum_{j=1}^N H_{ij} \exp \hat{a}_j \cos[(\Theta_{ij} \hat{v}_j)], \quad (19)$$

$$\{g_S(\hat{a}, \hat{v})\}_i := \sum_{j=1}^N H_{ij} \exp \hat{a}_j \sin[(\Theta_{ij} \hat{v}_j)], \quad (20)$$

where  $H$  is the geometry matrix with dimensions  $M \times N$ ,  $M$  is the number of measurement points (pixels),  $N$  is the number of discretized points in the plasma domain, and  $\Theta_{ij}$  is the directional cosine factor corresponding to  $\vec{v} \cdot \vec{l} / |\vec{v}| |\vec{l}|$  for the  $i$ -th measurement and  $j$ -th point.

To explicitly indicate that the data are observed and not random variables, superscripts with "obs" notation are introduced, as in the following equations:

$$\mathbf{I}_0^{\text{obs}} = \mathbf{g}_0(\hat{e}) + \epsilon_0, \quad (21)$$

$$\mathbf{I}_{\text{Re}}^{\text{obs}} = \mathbf{g}_C(\hat{a}, \hat{v}) + \epsilon_1, \quad \mathbf{I}_{\text{Im}}^{\text{obs}} = \mathbf{g}_S(\hat{a}, \hat{v}) + \epsilon_1, \quad (22)$$

which are acquired from  $I_0$ ,  $\text{Re}(I_D)$ , and  $\text{Im}(I_D)$ , respectively. Here,  $\epsilon_0$  and  $\epsilon_1$  represent measurement noise in the observations, assumed to be normally distributed with zero mean and covariances  $\Sigma_0$  and  $\Sigma_1$ , respectively.

## IV. NONLINEAR GAUSSIAN PROCESS TOMOGRAPHY FOR THE CIS MODEL

### A. Bayesian Framework for Tomography

In this framework, the variables  $\hat{e}$ ,  $\hat{T}$ , and  $\hat{v}$  are modeled as Gaussian processes. Therefore, the discretized vectors of

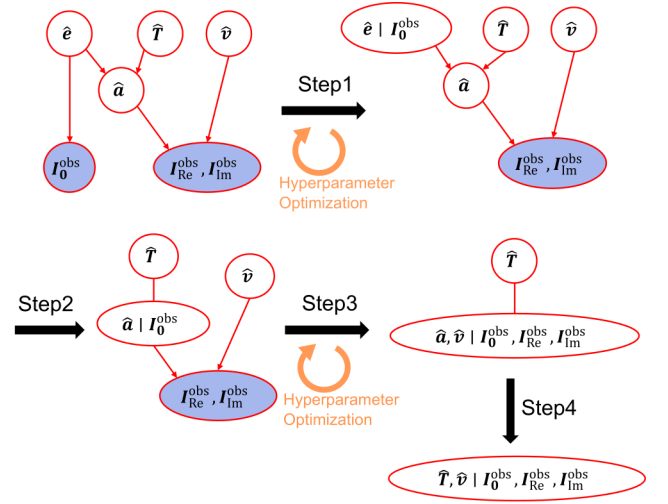


FIG. 2. Conceptual diagrams of the tomographic model for CIS. The first diagram is a directed Bayesian graphical model of the CIS projection equations, consisting of Eqs. (17), (18), (19), (20), (21), and (22). Each node represents a random variable, and the blue nodes are observed data. Step 1 computes the posterior probability of the log-emissivity  $\hat{e}$  given the observed data  $\mathbf{I}_0^{\text{obs}}$ . Step 2 marginalizes the variable  $\hat{e}$ . Step 3 computes the posterior probabilities of  $\hat{a}$  and  $\hat{v}$ . Step 4 marginalizes the variable  $\hat{a}$ .

these variables follow multivariate Gaussian distributions, denoted as:

$$p(\hat{e}) = \mathcal{N}(\hat{e} | \mu_e^{\text{pri}}, K_e),$$

$$p(\hat{T}) = \mathcal{N}(\hat{T} | \mu_T^{\text{pri}}, K_T),$$

$$p(\hat{v}) = \mathcal{N}(\hat{v} | \mu_v^{\text{pri}}, K_v),$$

where  $\mu_e^{\text{pri}}$ ,  $\mu_T^{\text{pri}}$ , and  $\mu_v^{\text{pri}}$  are the prior mean vectors of the log-emissivity, temperature, and velocity, respectively, and  $K_e$ ,  $K_T$ ,  $K_v$  are the prior covariance matrices.

The goal of Bayesian estimation in this section is to find the posterior probability of the local variables  $\hat{T}$  and  $\hat{v}$  given the observed data from the CIS signals, yielding  $p(\hat{T}, \hat{v} | \mathbf{I}_0^{\text{obs}}, \mathbf{I}_{\text{Re}}^{\text{obs}}, \mathbf{I}_{\text{Im}}^{\text{obs}})$ . Although the variable  $\hat{e}$  seems unrelated to the primary objective, it significantly influences the tomography for temperature and velocity by mediating through the local amplitude  $\hat{a}$ , as defined in Eq. (17). Therefore, all three equations (Eqs. (18), (19), (20)) must be considered, and then the unnecessary variables  $\hat{e}$  and  $\hat{a}$  will be marginalized later, as described below:

$$\begin{aligned} & p(\hat{T}, \hat{v} | \mathbf{I}_0^{\text{obs}}, \mathbf{I}_{\text{Re}}^{\text{obs}}, \mathbf{I}_{\text{Im}}^{\text{obs}}) \\ &= \iint p(\hat{T}, \hat{v}, \hat{a}, \hat{e} | \mathbf{I}_0^{\text{obs}}, \mathbf{I}_{\text{Re}}^{\text{obs}}, \mathbf{I}_{\text{Im}}^{\text{obs}}) d\hat{a} d\hat{e} \\ &= \iint p(\hat{a}, \hat{v} | \mathbf{I}_{\text{Re}}^{\text{obs}}, \mathbf{I}_{\text{Im}}^{\text{obs}}) \delta(\hat{T} - \hat{e} + \hat{a}) p(\hat{e} | \mathbf{I}_0^{\text{obs}}) d\hat{a} d\hat{e}, \end{aligned} \quad (23)$$

where  $\delta(\cdot)$  is the Dirac delta function.

Since the straightforward calculation of Eq. (23) is still too complicated to solve, the following step-by-step procedure is

presented instead. A graphical representation of this procedure is shown in Fig. 2.

- **Step 1.** Calculate the approximate posterior probability of the log-emissivity  $\hat{e}$ . The relationship between the observed intensity  $\mathbf{I}_0^{\text{obs}}$  and the log-emissivity  $\hat{e}$  is isolated in Eq. (18), so the log-emissivity reconstruction can be performed independently of temperature and velocity. We numerically obtain the approximate posterior probability, denoted as

$$p(\hat{e} | \mathbf{I}_0^{\text{obs}}) \stackrel{\text{LA}}{\simeq} \mathcal{N}(\hat{e} | \tilde{\boldsymbol{\mu}}_e^{\text{LA}}, \tilde{\boldsymbol{\Sigma}}_e^{\text{LA}}). \quad (24)$$

- **Step 2.** Introduce the mediating variable  $\hat{\mathbf{a}}$ . Given that  $p(\hat{\mathbf{a}} | \hat{e}, \hat{\mathbf{T}}) = \delta(\hat{\mathbf{a}} - \hat{e} + \hat{\mathbf{T}})$ ,  $p(\hat{\mathbf{T}}) = \mathcal{N}(\hat{\mathbf{T}} | \boldsymbol{\mu}_T^{\text{pri}}, K_T)$ , and using Eq. (24) to obtain  $p(\hat{\mathbf{a}}, \hat{\mathbf{T}}, \hat{e} | \mathbf{I}_0^{\text{obs}})$ , we marginalize  $\hat{e}$  to derive the prior probability of  $\hat{\mathbf{a}}$  as follows:

$$p(\hat{\mathbf{a}} | \mathbf{I}_0^{\text{obs}}) = \mathcal{N}(\hat{\mathbf{a}} | \tilde{\boldsymbol{\mu}}_a^{\text{LA}} - \boldsymbol{\mu}_T^{\text{pri}}, \tilde{\boldsymbol{\Sigma}}_a^{\text{LA}} + K_T). \quad (25)$$

We denote  $\boldsymbol{\mu}_a^{\text{pri}} := \tilde{\boldsymbol{\mu}}_a^{\text{LA}} - \boldsymbol{\mu}_T^{\text{pri}}$  and  $\boldsymbol{\Sigma}_a^{\text{pri}} := \tilde{\boldsymbol{\Sigma}}_a^{\text{LA}} + K_T$ .

- **Step 3.** Calculate the approximate posterior probability of  $\hat{\mathbf{a}}$  and  $\hat{\mathbf{v}}$  using the Laplace approximation. The details of the Laplace approximation are described in the next subsection. Here,  $\hat{\mathbf{a}} \sim \mathcal{N}(\boldsymbol{\mu}_a^{\text{pri}}, \boldsymbol{\Sigma}_a^{\text{pri}})$  and  $\hat{\mathbf{v}} \sim \mathcal{N}(\boldsymbol{\mu}_v^{\text{pri}}, K_v)$  are used as the priors for the CIS model. The resulting approximate posterior probabilities are denoted as:

$$p(\hat{\mathbf{a}}, \hat{\mathbf{v}} | \mathbf{I}_0^{\text{obs}}, \mathbf{I}_{\text{Re}}^{\text{obs}}, \mathbf{I}_{\text{Im}}^{\text{obs}}) \stackrel{\text{LA}}{\simeq} \mathcal{N}\left(\begin{pmatrix} \hat{\mathbf{a}} \\ \hat{\mathbf{v}} \end{pmatrix} \middle| \begin{pmatrix} \tilde{\boldsymbol{\mu}}_a^{\text{LA}} \\ \tilde{\boldsymbol{\mu}}_v^{\text{LA}} \end{pmatrix}, \begin{bmatrix} \tilde{\boldsymbol{\Sigma}}_{aa}^{\text{LA}} & \tilde{\boldsymbol{\Sigma}}_{av}^{\text{LA}} \\ \tilde{\boldsymbol{\Sigma}}_{va}^{\text{LA}} & \tilde{\boldsymbol{\Sigma}}_{vv}^{\text{LA}} \end{bmatrix}\right).$$

- **Step 4.** Marginalize  $\hat{\mathbf{a}}$  to obtain the posterior of  $\hat{\mathbf{T}}$  and  $\hat{\mathbf{v}}$ . Consequently, when the final posterior probabilities are denoted as:

$$p(\hat{\mathbf{T}}, \hat{\mathbf{v}} | \mathbf{I}_0^{\text{obs}}, \mathbf{I}_{\text{Re}}^{\text{obs}}, \mathbf{I}_{\text{Im}}^{\text{obs}}) = \mathcal{N}\left(\begin{pmatrix} \hat{\mathbf{T}} \\ \hat{\mathbf{v}} \end{pmatrix} \middle| \begin{pmatrix} \tilde{\boldsymbol{\mu}}_T \\ \tilde{\boldsymbol{\mu}}_v \end{pmatrix}, \begin{bmatrix} \tilde{\boldsymbol{\Sigma}}_{TT} & \tilde{\boldsymbol{\Sigma}}_{Tv} \\ \tilde{\boldsymbol{\Sigma}}_{vT} & \tilde{\boldsymbol{\Sigma}}_{vv} \end{bmatrix}\right),$$

their mean vectors and covariance matrices are calculated using the following equations:

$$\begin{aligned} \tilde{\boldsymbol{\mu}}_T &= \boldsymbol{\mu}_T^{\text{pri}} + K_T[\boldsymbol{\Sigma}_a^{\text{pri}}]^{-1}(\tilde{\boldsymbol{\mu}}_e^{\text{LA}} - \boldsymbol{\mu}_T^{\text{pri}} - \tilde{\boldsymbol{\mu}}_a^{\text{LA}}), \\ \tilde{\boldsymbol{\mu}}_v &= \tilde{\boldsymbol{\mu}}_v^{\text{LA}}, \\ \tilde{\boldsymbol{\Sigma}}_{TT} &= K_T[\boldsymbol{\Sigma}_a^{\text{pri}}]^{-1}\tilde{\boldsymbol{\Sigma}}_e^{\text{LA}} + K_T[\boldsymbol{\Sigma}_a^{\text{pri}}]^{-1}\tilde{\boldsymbol{\Sigma}}_{aa}^{\text{LA}}[\boldsymbol{\Sigma}_a^{\text{pri}}]^{-1}K_T, \\ \tilde{\boldsymbol{\Sigma}}_{Tv} &= -K_T[\boldsymbol{\Sigma}_a^{\text{pri}}]^{-1}\tilde{\boldsymbol{\Sigma}}_{av}^{\text{LA}} = \tilde{\boldsymbol{\Sigma}}_{vT}^{\text{T}}, \\ \tilde{\boldsymbol{\Sigma}}_{vv} &= \tilde{\boldsymbol{\Sigma}}_{vv}^{\text{LA}}. \end{aligned} \quad (26)$$

## B. Laplace Approximation

As shown in Step 1 and Step 3 of the previous subsection, the Laplace approximation is used to compute the posterior probability of the local variables  $\hat{e}$ ,  $\hat{\mathbf{a}}$ , and  $\hat{\mathbf{v}}$  in the CIS model.

In the case of the log-emissivity  $\hat{e}$ , the log-posterior function  $\Psi^{\text{emit}}(\hat{e})$  is defined using Eqs. (18) and (21) as follows:

$$\begin{aligned} \Psi^{\text{emit}}(\hat{e}) &= \log p(\hat{e} | \mathbf{I}_0^{\text{obs}}) + C \\ &= -\frac{1}{2}(\mathbf{g}_0(\hat{e}) - \mathbf{I}_0^{\text{obs}})^{\text{T}}\boldsymbol{\Sigma}_{g_0}^{-1}(\mathbf{g}_0(\hat{e}) - \mathbf{I}_0^{\text{obs}}) \\ &\quad -\frac{1}{2}(\hat{e} - \boldsymbol{\mu}_e^{\text{pri}})^{\text{T}}K_e^{-1}(\hat{e} - \boldsymbol{\mu}_e^{\text{pri}}), \end{aligned}$$

where  $\boldsymbol{\Sigma}_{g_0}$  is the covariance matrix of the measurement error  $\epsilon_0$  described in Eq. (21), and  $C$  is a constant term that does not depend on  $\hat{e}$ .

Using matrix calculus, the analytical expressions of the gradient  $\nabla\Psi^{\text{emit}}(\hat{e})$  and the Hessian  $\nabla^2\Psi^{\text{emit}}(\hat{e})$  are derived as follows:

$$\begin{aligned} \{\nabla\Psi^{\text{emit}}(\hat{e})\}_i &= \left\{H^{\text{T}}\boldsymbol{\Sigma}_{g_0}^{-1}(\mathbf{g}_0(\hat{e}) - \mathbf{I}_0^{\text{obs}})\right\}_i \exp\hat{e}_i \\ &\quad - \left\{K_e^{-1}(\hat{e} - \boldsymbol{\mu}_e^{\text{pri}})\right\}_i, \quad (27) \\ \{\nabla^2\Psi^{\text{emit}}(\hat{e})\}_{ij} &= [H^{\text{T}}\boldsymbol{\Sigma}_{g_0}^{-1}H]_{ij} \exp\hat{e}_i \exp\hat{e}_j \\ &\quad - \delta_{ij} \left\{H^{\text{T}}\boldsymbol{\Sigma}_{g_0}^{-1}(\mathbf{g}_0(\hat{e}) - \mathbf{I}_0^{\text{obs}})\right\}_i \exp\hat{e}_i \\ &\quad - \{K_e^{-1}\}_{ij}, \quad (28) \end{aligned}$$

where  $i, j$  are indices of the vectors or matrices, and  $\delta_{ij}$  is the Kronecker delta. By substituting Eqs. (27) and (28) into Eq. (9) and iterating until convergence is achieved, we use Eqs. (7) and (8) to obtain the approximate mean vector  $\tilde{\boldsymbol{\mu}}_e^{\text{LA}}$  and the approximate covariance matrix  $\tilde{\boldsymbol{\Sigma}}_e^{\text{LA}}$  of the posterior probability.

For the local amplitude  $\hat{\mathbf{a}}$  and local velocity  $\hat{\mathbf{v}}$ , the log-posterior function  $\Psi^{\text{CIS}}(\hat{\mathbf{a}}, \hat{\mathbf{v}})$  is described using Eqs. (19), (20), and (22) as follows:

$$\begin{aligned} \Psi^{\text{CIS}}(\hat{\mathbf{a}}, \hat{\mathbf{v}}) &:= \log p(\hat{\mathbf{a}}, \hat{\mathbf{v}} | \mathbf{I}_{\text{Re}}^{\text{obs}}, \mathbf{I}_{\text{Im}}^{\text{obs}}) - C \\ &= -\frac{1}{2}(\mathbf{g}_C(\hat{\mathbf{a}}, \hat{\mathbf{v}}) - \mathbf{I}_{\text{Re}}^{\text{obs}})^{\text{T}}\boldsymbol{\Sigma}_{g_1}^{-1}(\mathbf{g}_C(\hat{\mathbf{a}}, \hat{\mathbf{v}}) - \mathbf{I}_{\text{Re}}^{\text{obs}}) \\ &\quad -\frac{1}{2}(\mathbf{g}_S(\hat{\mathbf{a}}, \hat{\mathbf{v}}) - \mathbf{I}_{\text{Im}}^{\text{obs}})^{\text{T}}\boldsymbol{\Sigma}_{g_1}^{-1}(\mathbf{g}_S(\hat{\mathbf{a}}, \hat{\mathbf{v}}) - \mathbf{I}_{\text{Im}}^{\text{obs}}) \\ &\quad -\frac{1}{2}(\hat{\mathbf{a}} - \boldsymbol{\mu}_a^{\text{pri}})^{\text{T}}(\boldsymbol{\Sigma}_a^{\text{pri}})^{-1}(\hat{\mathbf{a}} - \boldsymbol{\mu}_a^{\text{pri}}) \\ &\quad -\frac{1}{2}(\hat{\mathbf{v}} - \boldsymbol{\mu}_v^{\text{pri}})^{\text{T}}K_v^{-1}(\hat{\mathbf{v}} - \boldsymbol{\mu}_v^{\text{pri}}), \end{aligned}$$

where  $\boldsymbol{\Sigma}_{g_1}$  is the covariance matrix of the observation error  $\epsilon_1$  described in Eq. (22), and  $C$  is a constant term that does not depend on  $\hat{\mathbf{a}}$  and  $\hat{\mathbf{v}}$ .

The calculation procedure is analogous to that for the log-emissivity, but it should be noted that the total size of variables is doubled because joint probabilities of  $\hat{\mathbf{a}}$  and  $\hat{\mathbf{v}}$  are considered. In this case, we define the gradient and Hessian of the log-posterior function  $\Psi^{\text{CIS}}(\hat{\mathbf{a}}, \hat{\mathbf{v}})$  as block matrices:

$$\nabla\Psi^{\text{CIS}}(\hat{\mathbf{a}}, \hat{\mathbf{v}}) = \begin{bmatrix} \frac{\partial}{\partial \hat{\mathbf{a}}} \\ \frac{\partial}{\partial \hat{\mathbf{v}}} \end{bmatrix} \Psi^{\text{CIS}}(\hat{\mathbf{a}}, \hat{\mathbf{v}}), \quad (29)$$

$$\nabla^2\Psi^{\text{CIS}}(\hat{\mathbf{a}}, \hat{\mathbf{v}}) = \begin{bmatrix} \frac{\partial^2}{\partial \hat{\mathbf{a}} \partial \hat{\mathbf{a}}} & \frac{\partial^2}{\partial \hat{\mathbf{a}} \partial \hat{\mathbf{v}}} \\ \frac{\partial^2}{\partial \hat{\mathbf{v}} \partial \hat{\mathbf{a}}} & \frac{\partial^2}{\partial \hat{\mathbf{v}} \partial \hat{\mathbf{v}}} \end{bmatrix} \Psi^{\text{CIS}}(\hat{\mathbf{a}}, \hat{\mathbf{v}}). \quad (30)$$

Due to the presence of the directional cosine matrix  $\Theta$ , the specifics of Eqs. (29) and (30) are complex and are detailed in Appendix C. The components of the gradient are given in Eqs. (C1) and (C1), and the components of the Hessian are given in Eqs. (C3), (C4), and (C5).

### C. Hyperparameter Optimization

In the Bayesian framework, the hyperparameters of the Gaussian process priors, such as the prior mean vectors and covariance matrices ( $\mu_e^{\text{pri}}, K_e, \mu_T^{\text{pri}}, K_T, \mu_v^{\text{pri}}, K_v$ ), as well as the observation noise covariance matrices ( $\Sigma_{g_0}, \Sigma_{g_1}$ ), play a crucial role in the performance of the tomography. To determine appropriate values for these hyperparameters, we use the evidence approximation obtained via the Laplace approximation. By maximizing the approximate log-marginal likelihood with respect to the hyperparameters, we find their optimal values that best explain the observed data.

For the emission model, the approximate log-marginal likelihood  $\mathcal{L}^{\text{emit}}$  is given by:

$$\begin{aligned} \mathcal{L}^{\text{emit}}(\theta) = & \Psi^{\text{emit}}(\tilde{\mu}_e^{\text{LA}}) - \frac{1}{2} \log |K_e| - \frac{1}{2} \log |\Sigma_{g_0}| \\ & + \frac{1}{2} \log |\tilde{\Sigma}_e^{\text{LA}}|, \end{aligned} \quad (31)$$

where  $\theta = \{\mu_e^{\text{pri}}, K_e, \Sigma_{g_0}\}$  represents the set of hyperparameters for the emissivity model. In this equation,  $\Psi^{\text{emit}}(\tilde{\mu}_e^{\text{LA}})$  is the log-posterior function evaluated at the Laplace approximation mean  $\tilde{\mu}_e^{\text{LA}}$ .

Similarly, for the CIS model, the approximate log-marginal likelihood  $\mathcal{L}^{\text{CIS}}$  is given by:

$$\begin{aligned} \mathcal{L}^{\text{CIS}}(\theta) = & \Psi^{\text{CIS}}(\tilde{\mu}_a^{\text{LA}}, \tilde{\mu}_v^{\text{LA}}) - \frac{1}{2} \log |\tilde{\Sigma}_e^{\text{LA}} + K_T| - \frac{1}{2} \log |K_v| \\ & - \log |\Sigma_{g_1}| + \frac{1}{2} \log \left| \begin{array}{cc} \tilde{\Sigma}_{aa}^{\text{LA}} & \tilde{\Sigma}_{av}^{\text{LA}} \\ \tilde{\Sigma}_{va}^{\text{LA}} & \tilde{\Sigma}_{vv}^{\text{LA}} \end{array} \right|, \end{aligned} \quad (32)$$

where  $\theta = \{\mu_a^{\text{pri}}, \mu_v^{\text{pri}}, \Sigma_a^{\text{pri}}, K_v, \Sigma_{g_1}\}$  represents the set of hyperparameters for the CIS model. Here,  $\Psi^{\text{CIS}}(\tilde{\mu}_a^{\text{LA}}, \tilde{\mu}_v^{\text{LA}})$  is the log-posterior function evaluated at the Laplace approximation means  $\tilde{\mu}_a^{\text{LA}}$  and  $\tilde{\mu}_v^{\text{LA}}$ .

By maximizing  $\mathcal{L}^{\text{emit}}(\theta)$  and  $\mathcal{L}^{\text{CIS}}(\theta)$  with respect to the hyperparameters  $\theta$ , we can obtain their optimal values. This procedure ensures that the Gaussian process models for the log-emissivity, temperature, and velocity are appropriately tuned to the observed data, improving the accuracy and reliability of the tomographic reconstructions.

## V. TEST WITH PHANTOM DATA

### A. Configuration of the Tomographic Model for RT-1

In this study, we simulate observations of the plasma in the RT-1 experimental device using CIS<sup>6</sup>. Unlike confinement devices such as tokamaks and stellarators, RT-1 has only a

poloidal magnetic field and achieves pure axisymmetry. In this sense, RT-1 is more suitable for reconstruction from a single image. The CIS installed in RT-1 is shown in Fig. 3(a), with a tangential field of view to observe the toroidal flow. In this configuration, only the toroidal component of the flow is assumed.

The trajectories of the rays emanating from the camera are shown in Fig. 3(b). The positions of the local variables  $f$  are defined as  $\mathbf{f} = f(\vec{r})$ . In both conventional tomography methods and traditional GPT, it is common to arrange each of the  $\{\vec{r}_i\}_{i=1}^N$  on a grid. However, in our method, as shown in Fig. 3(c), we arrange the points in a scatter plot that is not restricted to a grid shape. In Gaussian processes naturally defined in function space, it is not necessary to arrange the points on a grid. Moreover, by varying the density of the point cloud, we can reduce the dimensionality of  $\mathbf{f}$  and decrease the computational cost. The reason for adopting such an arrangement is that, in the RT-1 plasma, the local structure becomes more complex closer to the levitated coil within the magnetic surfaces, requiring higher resolution in those regions.

Regarding the length scale for the kernel function, we adopt an isotropic but non-uniform one. To adjust the parameters, we express  $\ell(\vec{r})$  to substitute into the Gibbs kernel [Eq. (2)] as follows:

$$\ell(\vec{r}) = \hat{\ell}_F \ell'(\vec{r}), \quad (33)$$

where  $\ell'(\vec{r})$  is a non-uniform function given in Fig. 3(d), and  $\hat{\ell}_F$  is the length scale factor chosen to maximize the evidence. However, since the distance intervals of the point cloud in Fig. 3(c) correlate with  $\ell(\vec{r})$ , too small a length scale would result in insufficient degrees of freedom. Therefore, we impose the constraint  $\hat{\ell}_F > 1$  during the optimization.

As boundary conditions, we define the boundary local variable vector  $\mathbf{f}^{\text{bd}} = f(\vec{r}^{\text{bd}})$  from the orange point set in Fig. 3(c), and update the prior distribution  $\mu_f^{\text{pri}}$  and  $K_f^{\text{pri}}$  as the conditional probability given the values at  $\mathbf{f}^{\text{bd}}$ . Here, we set the values of temperature  $\hat{T}$  and velocity  $\hat{v}$  at the boundary to zero, and for the log-emissivity  $\hat{e}$ , we assign values in the range of  $-5$  to  $-3$ .

Regarding  $\Sigma_{g_0}$  and  $\Sigma_{g_1}$  necessary to define the likelihood function, in this test, we use artificial noise assumed to be uniform white Gaussian noise. Therefore, we assume an identity matrix scaled by the noise variance:

$$\Sigma_g = \sigma_g^2 I, \quad (34)$$

where  $\sigma_g$  is the sigma scale chosen to maximize the evidence, similar to  $\hat{\ell}_F$ .

### B. Phantom Data

The phantom distributions of emissivity, temperature, and velocity are shown in panels (a), (b), and (c) of Fig. 4, denoted as  $e_{\text{true}}$ ,  $\hat{T}_{\text{true}}$ , and  $\hat{v}_{\text{true}}$ , respectively. These distributions are based on the assumption that the plasma emits in a ring shape, with high temperature inside the ring, and the velocity

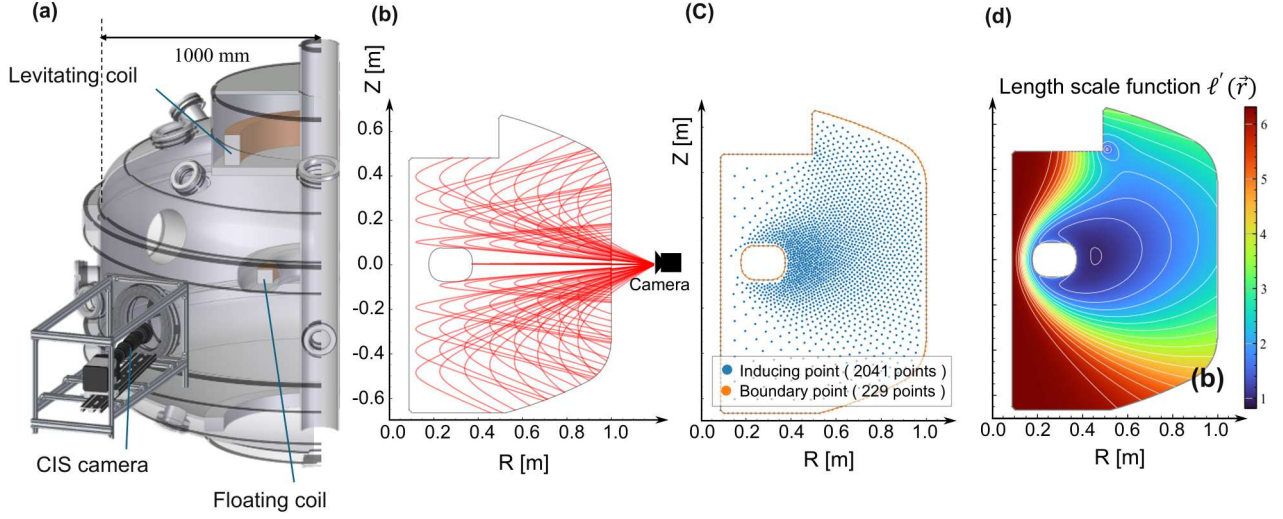


FIG. 3. (a) A conceptual diagram of the camera system in RT-1, where the CIS camera is installed tangentially to the plasma cross-section to detect toroidal flow. (b) Examples of projected lines of rays (the red lines) from the camera on the poloidal cross-section of RT-1. The number of rays is reduced for simplicity. (c) The distribution of scattered inducing points  $\vec{r}^{idc}$  (the blue points) and boundary points  $\vec{r}^{bd}$  (the orange points). The number of inducing points is 2041, and the number of boundary points is 229 in the setup. (d) The length scale function  $\ell'(\vec{r})$  in RT-1. These conditions are consistent with previous work<sup>22</sup>.

switches between positive and negative at the boundary of the ring. Note that these patterns are not directly related to the actual observations in RT-1.

The input data for the test are generated using Eqs. (18) and (21) for the emissivity (panel d), and Eqs. (19), (20), and (22) for the real and imaginary components (panels e and f), with the phantom distributions as inputs. The results are shown in panels (d), (e), and (f) of Fig. 4, denoted as  $I_0^{inp}$ ,  $I_{Re}^{inp}$ , and  $I_{Im}^{inp}$ , respectively.

Panels (g) and (h) in Fig. 4 represent the projected temperature and velocity, which are calculated by:

$$\hat{T}_D = \log \sqrt{\frac{I_0^2}{I_{Re}^2 + I_{Im}^2}}, \quad \hat{v}_D = \arctan \frac{I_{Im}}{I_{Re}}, \quad (35)$$

and correspond to  $\log \zeta_D$  and  $\phi_D$  in Eq. (10), respectively.

In contrast to the relationship between the emissivity of the projected image [Fig. 4(d)] and the phantom distribution [Fig. 4(a)], Figs. 4(g) and 4(h) indicate that for temperature and velocity, it is difficult for humans to infer the original distributions from the projected images. This is because the three physical variables influence each other through the integration process, resulting in more complex outputs. Additionally, we emphasize that the peak values of both the normalized temperature  $\hat{T}$  and normalized velocity  $\hat{v}$  are set to be around 2. These values are sufficiently high that linear approximations are invalid.

To validate the tomography, artificial noise is added to the generated projection images as input data. The noise is uniform white Gaussian noise, and the noise level is set to 10% for  $I_0$  and 2% for  $I_{Re}$  and  $I_{Im}$ . The noise level is defined as the ratio of the standard deviation of the white noise to the mean of  $I_0$ .

### C. Results of the Test

Based on the hyperparameters  $\mu_e^{pri}$ ,  $K_e$ ,  $\Sigma_{g_0}$ ,  $\mu_T^{pri}$ ,  $K_T$ ,  $\mu_v^{pri}$ ,  $K_v$ , and  $\Sigma_{g_1}$ , and input images  $I_0^{inp}$ ,  $I_{Re}^{inp}$ ,  $I_{Im}^{inp}$ , we perform the tomography using the nonlinear GPT for CIS described in Sec. IV. For hyperparameter optimization, there are two objective functions,  $\mathcal{L}^{emit}$  and  $\mathcal{L}^{CIS}$ , which are given in Eqs. (31) and (32), respectively. Before proceeding to Step 2,  $\mathcal{L}^{emit}$  is optimized, and the optimal  $\tilde{\mu}_e^{LA}$  and  $\tilde{\Sigma}_e^{LA}$  are used in Step 2. Then, the optimization of  $\mathcal{L}^{CIS}$  is performed in Step 3. Finally, we obtain the mean vectors  $\tilde{\mu}_T$  and  $\tilde{\mu}_v$ , and covariance matrices  $\tilde{\Sigma}_{TT}$ ,  $\tilde{\Sigma}_{Tv}$ ,  $\tilde{\Sigma}_{vT}$ , and  $\tilde{\Sigma}_{vv}$ .

Figure 5 shows the evidence maps of  $\mathcal{L}^{emit}$  and  $\mathcal{L}^{CIS}$  with respect to the length scale factor  $\hat{\ell}_F$  and the sigma scale  $\sigma_g$ . The optimal values are obtained at  $(\hat{\ell}_F, \sigma_{g_0}) = (1.71, 9.7\%)$  for the emissivity model, and at  $(\hat{\ell}_F, \sigma_{g_1}) = (1.86, 1.9\%)$  for the CIS model. Regarding the sigma scale, the optimal values are almost the same as the noise levels, which are 10% for  $I_0$  and 2% for  $I_{Re}$  and  $I_{Im}$ , indicating that the noise levels can be predicted by maximizing the evidence when the error follows white Gaussian noise.

Tomographic results with optimal hyperparameters are shown in Fig. 6, where the distributions of temperature and velocity on the poloidal cross-section of RT-1 are displayed. The mean values of the posterior temperature and velocity,  $\tilde{\mu}_T$  and  $\tilde{\mu}_v$ , are shown in panels (a) and (e) of Fig. 6, respectively. Error values, calculated as  $\tilde{\mu}_T - \hat{T}_{true}$  and  $\tilde{\mu}_v - \hat{v}_{true}$ , are shown in panels (b) and (f), respectively. Standard deviations of the posterior temperature and velocity, given by

$$\{\tilde{\sigma}_T\}_i = [\tilde{\Sigma}_{TT}]_{ii}^{1/2}, \quad \{\tilde{\sigma}_v\}_i = [\tilde{\Sigma}_{vv}]_{ii}^{1/2},$$

are shown in panels (c) and (g), respectively.

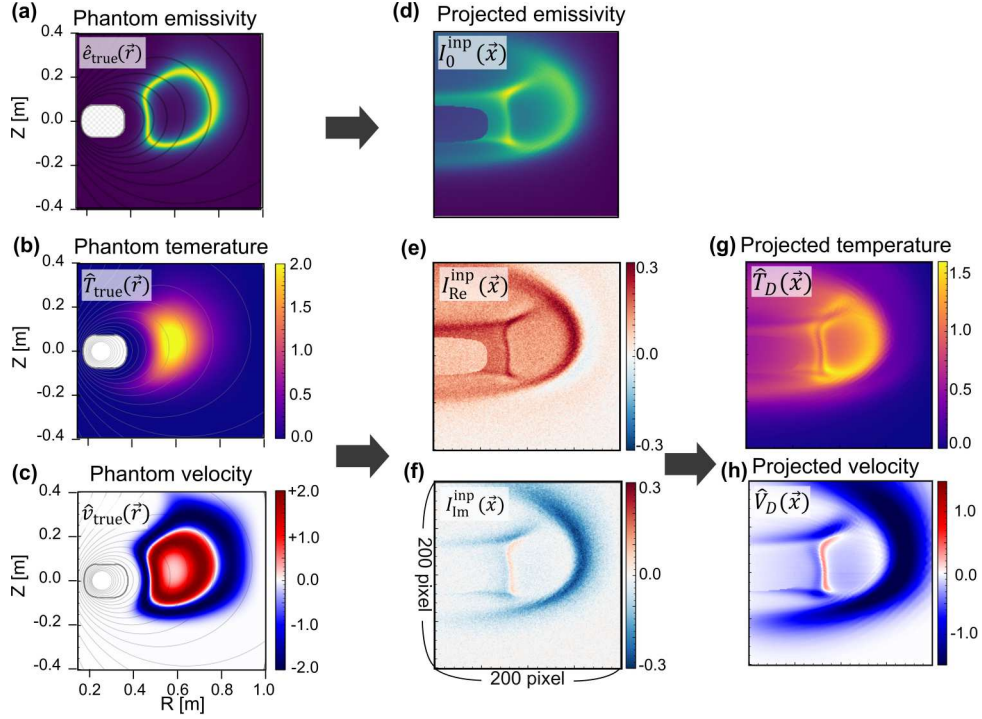


FIG. 4. Phantom data for the test tomography and the corresponding projected images. The left column, (a), (b), and (c), are phantom distributions of local emissivity ( $e_{\text{true}}$ ), local temperature ( $\hat{T}_{\text{true}}$ ), and local velocity ( $\hat{v}_{\text{true}}$ ), respectively. Panel (d) is the projected emissivity,  $I_0^{\text{inp}}$ , using Eqs. (18) and (21). Panels (e) and (f) are input images for CIS tomography generated by Eqs. (19), (20), and (22), corresponding to  $I_{\text{Re}}^{\text{inp}}$  and  $I_{\text{Im}}^{\text{inp}}$ , respectively. Panels (g) and (h) are the projected temperature and projected velocity, respectively.

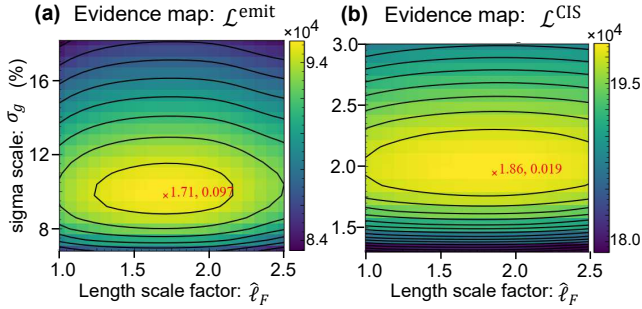


FIG. 5. Evidence maps for the CIS tomography model when the input images are shown in Fig. 4. (a)  $\mathcal{L}^{\text{emit}}$  and (b)  $\mathcal{L}^{\text{CIS}}$  are defined in Eqs. (31) and (32), respectively. The horizontal and vertical axes represent the length scale factor  $\hat{\ell}_F$  and the sigma scale  $\sigma_g$ , which are defined in Eqs. (33) and (34), respectively. The red crosses indicate the maximum points.

Regions with large standard deviations of temperature and velocity correspond to regions of low emissivity, which is consistent with the property in CIS that spectral information is not propagated to the measurement in the absence of emissivity. Comparing the distributions of errors [(b), (f)] with the distributions of standard deviations [(c), (g)], the standard deviations roughly envelop the errors, which implies that the errors are predictable from the variance of the posterior probabilities.

These trends are also confirmed by the radial profiles at  $z = 0$  m, as shown in panels (d) and (h) of Fig. 6, which show that the temperature and velocity deviate from the true values due to low emission in the range of  $0.5 \text{ m} < R < 0.7 \text{ m}$ , but this is compensated for by the increase in the confidence interval.

## VI. TOMOGRAPHY WITH EXPERIMENTAL DATA

In this section, we present the tomographic reconstruction of ion temperature and velocity in the RT-1 device using data from the CIS diagnostic system. Details of the CIS system in RT-1 are described in Ref.<sup>7</sup>. The CIS cell used in this experiment has a  $\check{\phi}_0$  of 124.1 rad/nm, corresponding to a characteristic velocity  $v_c$  of 5.17 km/s and a characteristic temperature  $T_c$  of 2.23 eV for the He II line (468.58 nm). Figure 7 shows the field of view and installation of the CIS system.

The input images for the tomography model are shown in Fig. 8. Panel (a) shows the raw images, which were acquired three times under the same plasma discharge conditions with an exposure time of 0.5 s. Panel (b) shows a simulated image used for adjusting the location, focal length, and angle of view of the camera. Panels (d), (e), and (f) are the input images derived by Fourier analysis and calibration techniques<sup>7</sup>, corresponding to  $I_0^{\text{obs}}(\vec{x})$ ,  $I_{\text{Re}}^{\text{obs}}(\vec{x})$ , and  $I_{\text{Im}}^{\text{obs}}(\vec{x})$ , respectively. These input images are reduced in size from  $512 \times 512$  pixels to  $256 \times 256$  pixels for computational reasons.

In this tomography, instead of using Eq. (34), the sigma ma-



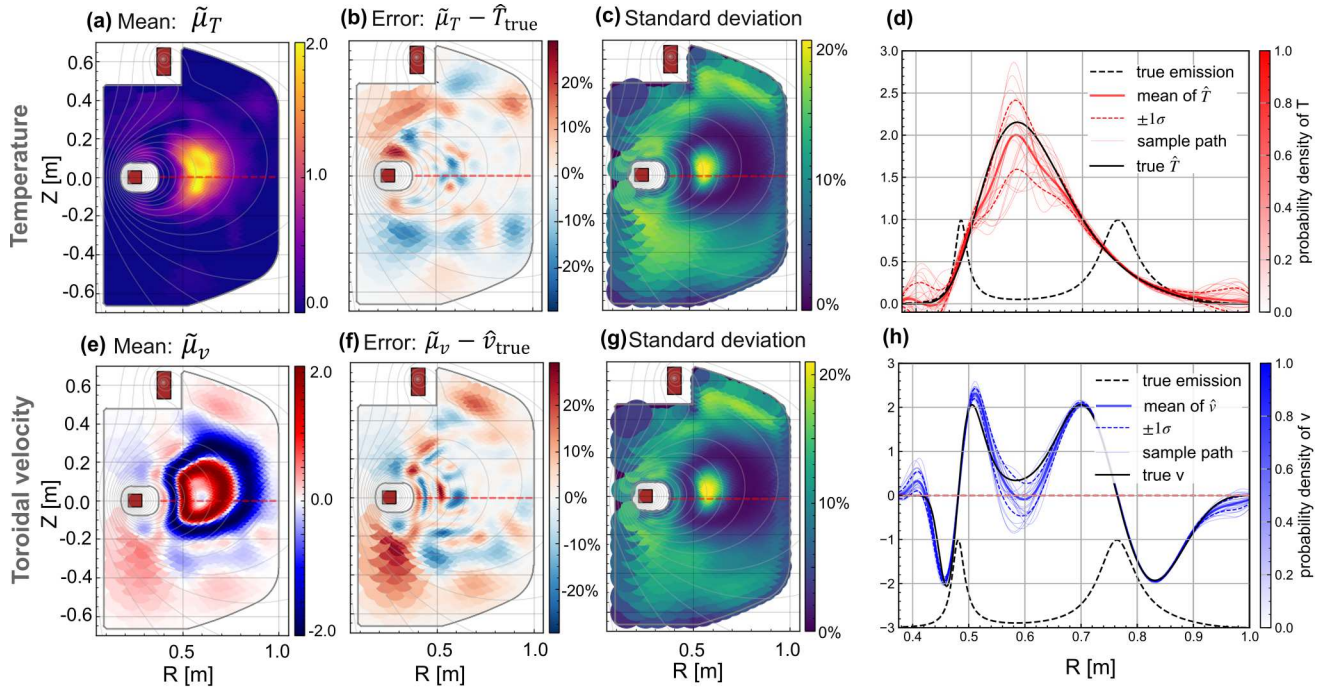


FIG. 6. The tomographic results of temperature and velocity with  $\sigma_g = 0.019$  and  $\hat{\ell}_F = 1.86$  when the phantom distributions and input images are shown in Fig. 4. The top row represents the temperature, and the bottom row represents the velocity. The first column, (a) and (e), shows the posterior means of each variable. The second column, (b) and (f), displays the errors given by the mean minus the true value. The third column, (c) and (g), presents the standard deviations of the posteriors. The rightmost column, (d) and (h), shows the radial profiles at  $z = 0$  m, where the black solid lines are the true values of each variable, black dashed lines are the true values of the emissivity, red and blue solid lines are the means of temperature and velocity, respectively, red and blue dashed lines are the  $-\sigma$  and  $+\sigma$  regions of the posterior probabilities of each variable, and thin colored lines are the sample paths of each posterior probability.

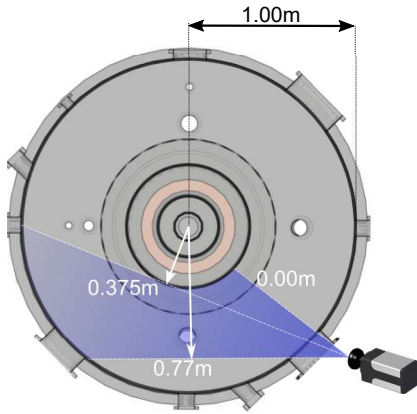


FIG. 7. Top view of the CIS field of view on the equatorial plane in RT-1.

trix for the likelihood function,  $\Sigma_g$ , is defined as the following diagonal matrix:

$$\Sigma_g = \sigma_g^2 \hat{\sigma}_g^2(\vec{x}), \quad (36)$$

where the relative sigma image  $\hat{\sigma}_g(\vec{x})$  is shown in Fig. 8(c). This image assigns relatively large values to regions affected by complex reflections, such as the inside of a viewing port or walls with positive Gaussian curvature. Unfortunately, unlike

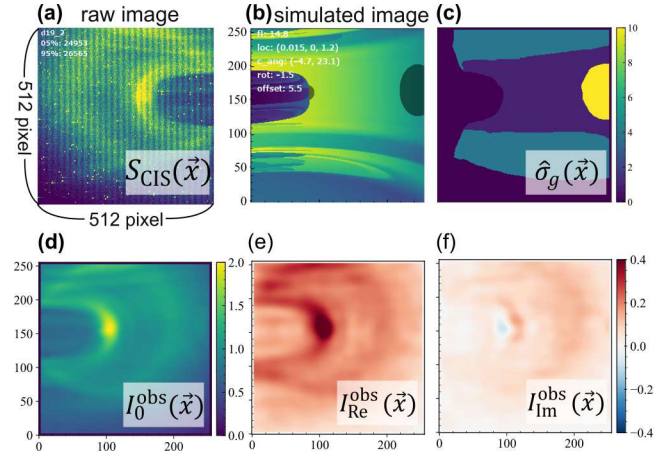


FIG. 8. Input images for CIS tomography. (a) Raw images measured by the CIS system. (b) Simulated image. (c) Relative sigma image  $\hat{\sigma}_g(\vec{x})$ . (d), (e), and (f) are the input images derived by Fourier analysis:  $I_0^{obs}(\vec{x})$ ,  $I_{Re}^{obs}(\vec{x})$ , and  $I_{Im}^{obs}(\vec{x})$ , respectively.

in Fig. 5, the optimized sigma scale could not be obtained through evidence maximization; both  $\sigma_g$  and  $\hat{\ell}_F$  converged to zero. This is because the diagonal matrix model for  $\Sigma_g$  only fits white noise and is unable to account for systematic errors such as reflections and geometric distortions. The input

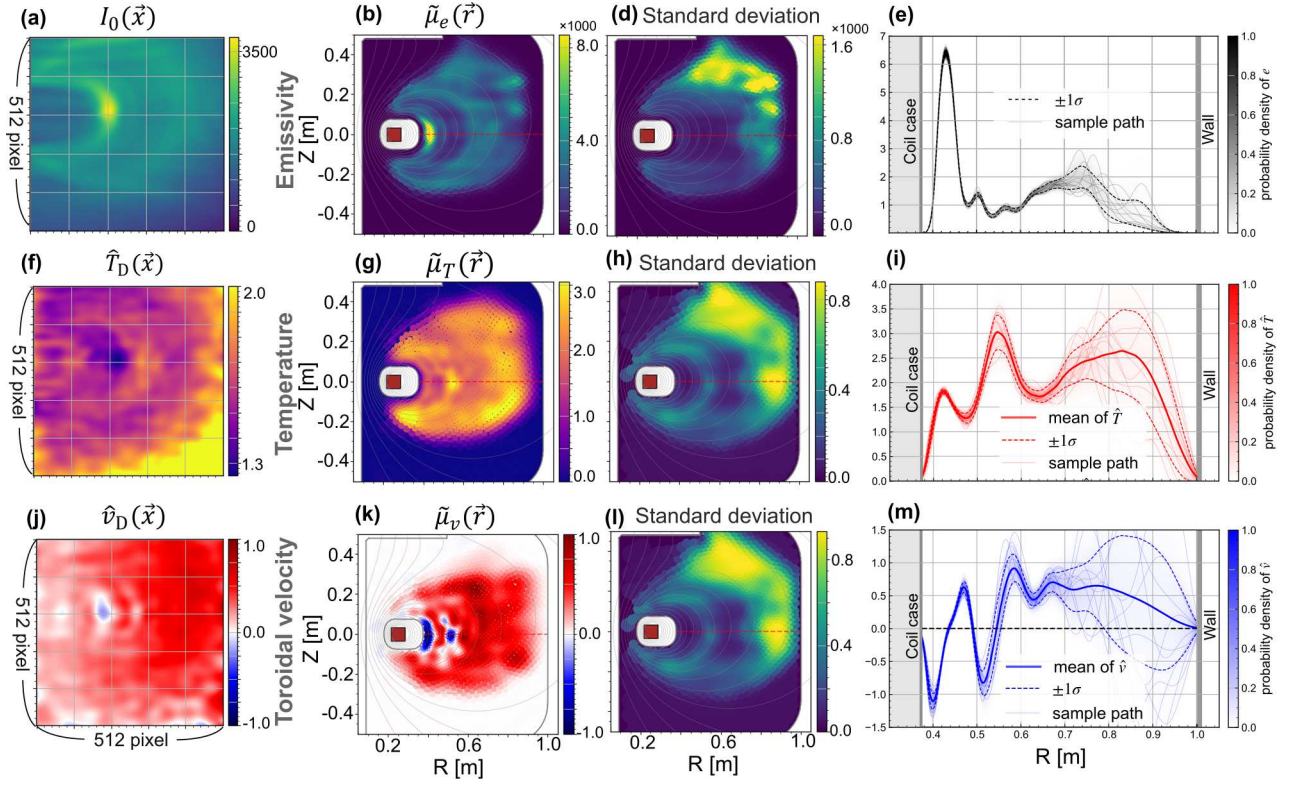


FIG. 9. Tomographic results with experimental data in RT-1. The first column, (a), (f), and (j), shows projected emissivity, ion temperature, and toroidal velocity, respectively. The second column, (b), (g), and (k), shows the mean of the posterior probabilities of emissivity, ion temperature, and toroidal velocity, respectively. The third column, (c), (h), and (l), shows the standard deviations of each physical quantity. The fourth column, (d), (i), and (m), shows the radial profiles of the mean distributions, where solid lines are the mean values, dashed lines are the  $-\sigma$  and  $+\sigma$  regions of each posterior probability, and thin colored lines are sample paths.

image, which was denoised by Fourier analysis, causes the sigma scale to converge to zero and leads to overfitting of the length scale to systematic noise. To include such systematic errors, the tomographic model should have accounted for how reflections and geometric errors propagate to the sigma matrix specifically, which was not done in this paper. Instead, we fixed the sigma scale at 10% and optimized only the length scale factor.

Figure 9 shows the results of the tomography, consisting of the posterior distributions of emissivity, ion temperature, and toroidal velocity when the length scale factor is optimized to 1.97. Panels (a), (f), and (j) show the projected emissivity, ion temperature, and toroidal velocity, respectively, obtained using Eq. (10). Panels (b), (g), and (k) show the mean distributions of emissivity, ion temperature, and toroidal velocity, respectively. Panels (c), (h), and (l) show the standard deviations of each physical quantity. The large standard deviations in the upper right regions of the poloidal cross-section are due to the relatively small number of rays or the propagation of the relative sigma image. From the radial profiles shown in panels (d), (i), and (m), the peak of the ion temperature and the sign structure of the ion velocity are observed in the region of  $0.4\text{ m} < R < 0.6\text{ m}$ . Also, the variances of  $T_i$  and  $V_i$  tend to be larger when the emissivity is relatively small, as in the case of the phantom data. Additionally, all physical quantities have

large variances in the region of  $R > 0.7\text{ m}$ , which is due to the fact that the LOS do not pass tangentially through this region, as shown in Fig. 7.

## Discussion

In this study, we chose the He II singlet line at 468.58 nm as the line of interest for Doppler spectroscopy, and we assumed that the ion flow is in the toroidal direction only. Extending the tomography to reconstruct three-dimensional velocity vectors would require increasing the number of velocity variables threefold to include  $v_\phi$ ,  $v_r$ , and  $v_z$ , as well as deriving the gradient and Hessian of the log-posterior function  $\Psi^{\text{CIS}}$  accordingly.

In general, impurity lines such as carbon (C III) are often used for Doppler spectroscopy in the SOL in CIS diagnostics. In such cases, it is necessary to consider multiplet spectra. As discussed in Appendix B, the effect of multiplets can be incorporated as a factor of complex numbers  $\gamma^{\text{mult}}(\vec{x})$  in the projection equation. As long as the intensity ratios of the spectral lines can be assumed to be constant along the LOS, the multiplet effect does not affect the integrand function of the projection equation.

Similarly, the Zeeman effect should be considered in high

magnetic field confinement devices for the temperature reconstruction<sup>29,30</sup>. It has been suggested that the Zeeman splitting can be approximated by a pseudo-temperature, such as  $\hat{T}_{\text{total}}(\vec{r}) \simeq \hat{T}_{\text{Zeeman}}(\vec{r}) + \hat{T}_i(\vec{r})$ , where  $\hat{T}_{\text{Zeeman}}$  represents the contribution from the Zeeman effect.

## VII. CONCLUSION

In this paper, we have developed a new Bayesian tomography framework that enables the simultaneous reconstruction of ion temperature and velocity in Coherence Imaging Spectroscopy (CIS). To incorporate the temperature effects and nonlinear influences that have been neglected in conventional CIS tomography, we adopted the approach of nonlinear Gaussian Process Tomography (GPT) using the Laplace approximation. By modeling the prior probabilities of log-emissivity, temperature, and velocity as Gaussian processes, we achieved the reconstruction of the local distributions of temperature and velocity while strictly maintaining the integral equations. This approach has, for the first time, addressed the previous challenges of velocity divergence in regions with low emissivity and the limitation of solvability only in linear regions where  $\hat{v}_i \ll 1$ .

The proposed tomography method was demonstrated using both phantom data and experimental data from the RT-1 device as a case study. The results showed that even in regions with strong nonlinearity where  $\hat{T}, \hat{v} \sim 2$ , reconstruction was possible within acceptable error margins in the phantom data. In the reconstruction using experimental data from RT-1, we successfully identified, for the first time, the spatial structures of ion temperature and toroidal ion flow characteristic of magnetospheric plasma.

This research has expanded the applicability of CIS tomography, making it possible to obtain posterior probabilities that include not only velocity but also temperature. This advancement not only allows for objective evaluation of the reliability of estimation results but also facilitates data integration with other diagnostics. By providing a comprehensive and statistically robust framework, the nonlinear GPT enhances the potential of CIS in plasma diagnostics.

## ACKNOWLEDGMENTS

This research was conducted as part of the author's Ph.D. program at the University of Tokyo. The authors would like to express their sincere gratitude to Professor Masaki Nishiura for his invaluable guidance and support throughout the course of this study. We also acknowledge the RT-1 team for their essential assistance with the experiments and data collection. This work was supported by JSPS KAKENHI Grants [Grant No. 19KK0073 and Grant No. 23K25857].

## Appendix A: Derivation of the Projection Equation for CIS

According to previous research<sup>8</sup>, the Coherence Imaging Spectroscopy (CIS) technique uses the principle of interference. The output signal  $S_{\text{CIS}}$  is the sum of the power of the incident light and its autocorrelation at a certain delay time  $\tau$ .

Given the power spectral density function of the coherent light  $\psi(\hat{\lambda})$ , where  $\hat{\lambda}$  is the normalized wavelength defined as  $\hat{\lambda} = \frac{\lambda - \lambda_0}{\lambda_0}$ , the interfered signal is written as follows:

$$S_{\text{CIS}}[\psi] = I_0[\psi] + \text{Re}(\Gamma[\psi]), \quad (\text{A1})$$

where  $I_0[\psi]$  is the total energy of the spectrum, and  $\Gamma[\psi]$  is the Fourier transform of the spectrum according to the Wiener–Khinchin theorem. The phase shift is given by

$$2\pi\nu\tau = \phi_0 - 2\pi\hat{N}\hat{\lambda}, \quad (\text{A2})$$

where  $\phi_0$  and  $\check{\phi}_0$  are constants related to the interferometer, and  $\nu$  is the frequency of the light.

The definitions of  $I_0[\psi]$  and  $\Gamma[\psi]$  are:

$$I_0[\psi] = \int_{-\infty}^{\infty} \psi(\hat{\lambda}) d\hat{\lambda}, \quad (\text{A3})$$

$$\Gamma[\psi] = \exp[i\phi_0] \int_{-\infty}^{\infty} \psi(\hat{\lambda}) \exp[-2\pi i\hat{N}\hat{\lambda}] d\hat{\lambda}. \quad (\text{A4})$$

Under the assumption that the spectrum of local emissivity has a single Gaussian profile with local amplitude  $e(\vec{r})$ , local wavelength shift  $\hat{\lambda}_D(\vec{r})$ , and local width  $\delta_D(\vec{r})$ , the spectrum of the incident light is obtained as the result of the line integral along the  $L(\vec{x})$  and is expressed as:

$$\psi(\vec{x}, \hat{\lambda}) = \int_{L(\vec{x})} \frac{e(\vec{r})}{\sqrt{2\pi\delta_D^2(\vec{r})}} \exp\left[-\frac{(\hat{\lambda} - \hat{\lambda}_D(\vec{r}))^2}{2\delta_D^2(\vec{r})}\right] dl. \quad (\text{A5})$$

Substituting Eq. (A5) into Eqs. (A3) and (A4),  $I_0(\vec{x})$  and  $\Gamma[\psi_{\vec{x}}]$  are derived by interchanging the order of integration:

$$I_0[\psi_{\vec{x}}] \equiv I_0(\vec{x}) = \int_{L(\vec{x})} e(\vec{r}) dl, \quad (\text{A6})$$

and

$$\begin{aligned} \Gamma[\psi_{\vec{x}}] &= \exp[i\phi_0(\vec{x})] \int_{L(\vec{x})} \int_{-\infty}^{\infty} \frac{e(\vec{r})}{\sqrt{2\pi\delta_D^2(\vec{r})}} \exp\left[-\frac{(\hat{\lambda} - \hat{\lambda}_D(\vec{r}))^2}{2\delta_D^2(\vec{r})}\right] \\ &\quad \times \exp[-2\pi i\hat{N}(\vec{x})\hat{\lambda}] d\hat{\lambda} dl \\ &= \exp[i\phi_0(\vec{x})] \int_{L(\vec{x})} e(\vec{r}) \\ &\quad \times \exp\left[-\frac{1}{2}(2\pi\hat{N}(\vec{x}))^2\delta_D^2(\vec{r}) + i2\pi\hat{N}(\vec{x})\hat{\lambda}_D(\vec{r})\right] dl \\ &\equiv \exp[i\phi_0(\vec{x})] I_D(\vec{x}). \end{aligned} \quad (\text{A7})$$

Under the assumption of a Maxwellian distribution, the local Doppler shift and broadening are related to the ion velocity  $v_i(\vec{r})$  and ion temperature  $T_i(\vec{r})$  by:

$$2\pi\hat{N}\hat{\lambda}_D(\vec{r}) = \frac{v_i(\vec{r}) \cdot \hat{l}}{v_c}, \quad \frac{1}{2}(2\pi\hat{N})^2\delta_D^2(\vec{r}) = \frac{T_i(\vec{r})}{T_c}, \quad (\text{A8})$$

where  $v_c$  and  $T_c$  are characteristic velocity and temperature, respectively, and  $\hat{l}$  is the unit vector along the LOS. Substituting Eq. (A8) into Eq. (A7), we obtain the projection equation used in CIS tomography.

### Appendix B: Projection Equation for the Multiplet Spectrum

We consider the function of the multiplet spectrum without Doppler shift and broadening as:

$$\psi^{\text{multi}}(\lambda) = e \sum_k C_k \delta(\lambda - \lambda_k), \quad (\text{B1})$$

where  $e$  is the total emissivity,  $\lambda_k$  is the wavelength of each line, and  $C_k$  is the relative intensity of each line satisfying  $\sum_k C_k = 1$ .

Under the assumption that  $C_k$  and  $\lambda_k$  are known and constant at each position  $\vec{r}$ , the shifted and broadened spectrum  $\psi^{\text{multi}}(\vec{r}, \hat{\lambda})$  at each  $\vec{r}$  is formulated as:

$$\psi^{\text{multi}}(\vec{r}, \hat{\lambda}) = e(\vec{r}) \sum_k \frac{C_k}{\sqrt{2\pi\delta_D^2(\vec{r})}} \exp\left(-\frac{(\hat{\lambda} - \lambda_k - \hat{\lambda}_D(\vec{r}))^2}{2\delta_D^2(\vec{r})}\right),$$

where  $\hat{\lambda}_k = \frac{\lambda_k - \lambda_0}{\lambda_0}$ . Substituting  $\psi^{\text{multi}}(\hat{\lambda}) = \int \psi^{\text{multi}}(\vec{r}, \hat{\lambda}) dl$  into Eq. (A4), we obtain:

$$\begin{aligned} \Gamma[\psi^{\text{multi}}] &= \exp[i\phi_0(\vec{x})] \gamma^{\text{multi}}(\vec{x}) \\ &\times \int_{L(\vec{x})} e(\vec{r}) \exp\left(-\frac{T_i(\vec{r})}{T_c} + i \frac{\mathbf{v}_i(\vec{r}) \cdot \hat{l}}{v_c}\right) dl, \end{aligned}$$

$$\text{where } \gamma^{\text{multi}}(\vec{x}) = \sum_k C_k \exp\left[i2\pi\hat{N}(\vec{x})\hat{\lambda}_k\right]. \quad (\text{B3})$$

Thus, in this case, the influence of the multiplet is summarized in the function  $\gamma^{\text{multi}}(\vec{x})$  and does not affect the integral process.

### Appendix C: Calculus for the log-posterior function of CIS

Using the Einstein summation convention, the gradient of the log-posterior distribution  $\nabla^2 \Psi^{\text{CIS}}(\vec{a}, \vec{v})$  is derived for each  $\vec{a}_j$  and  $\vec{v}_j$  as follows:

$$\begin{aligned} \frac{\partial}{\partial \vec{a}_j} \Psi^{\text{CIS}}(\vec{a}, \vec{v}) &= -\varepsilon_i^C \sigma_i^{-2} A_{ij}^C - \varepsilon_i^S \sigma_i^{-2} A_{ij}^S \\ &- \left[ \Sigma_a^{-1}(\vec{a} - \boldsymbol{\mu}_a^{\text{pri}}) \right]_j, \end{aligned} \quad (\text{C1})$$

$$\begin{aligned} \frac{\partial}{\partial \vec{v}_j} \Psi^{\text{CIS}}(\vec{a}, \vec{v}) &= +\varepsilon_i^C \sigma_i^{-2} \Theta_{ij} A_{ij}^S - \varepsilon_i^S \sigma_i^{-2} \Theta_{ij} A_{ij}^C \\ &- \left[ K_v^{-1}(\vec{v} - \boldsymbol{\mu}_v^{\text{pri}}) \right]_j, \end{aligned} \quad (\text{C2})$$

where the summation over  $i$  is implied, and the covariance matrix  $\Sigma_g$  is assumed to be diagonal,  $[\Sigma_g]_{ij} = \sigma_i^2 \delta_{ij}$ . The variables  $\varepsilon^C, \varepsilon^S, A^C$ , and  $A^S$  are given by:

$$\begin{aligned} A_{ij}^C &:= H_{ij} \exp(\vec{a}_j) \cos(\Theta_{ij} \vec{v}_j), \\ A_{ij}^S &:= H_{ij} \exp(\vec{a}_j) \sin(\Theta_{ij} \vec{v}_j), \\ \varepsilon_i^C &:= g_{C,i}(\vec{a}, \vec{v}) - I_{\text{Re},i}^{\text{obs}}, \\ \varepsilon_i^S &:= g_{S,i}(\vec{a}, \vec{v}) - I_{\text{Im},i}^{\text{obs}}. \end{aligned}$$

As a result, the following equations hold:

$$\begin{aligned} \frac{\partial g_{C,j}(\vec{a}, \vec{v})}{\partial \vec{a}_i} &= +A_{ji}^C, & \frac{\partial g_{S,j}(\vec{a}, \vec{v})}{\partial \vec{a}_i} &= +A_{ji}^S, \\ \frac{\partial g_{C,j}(\vec{a}, \vec{v})}{\partial \vec{v}_i} &= -\Theta_{ji} A_{ji}^S, & \frac{\partial g_{S,j}(\vec{a}, \vec{v})}{\partial \vec{v}_i} &= +\Theta_{ji} A_{ji}^C, \\ \frac{\partial A_{kj}^C}{\partial \vec{a}_i} &= +A_{kj}^C \delta_{ij}, & \frac{\partial A_{kj}^S}{\partial \vec{a}_i} &= +A_{kj}^S \delta_{ij}, \\ \frac{\partial A_{kj}^C}{\partial \vec{v}_i} &= -\Theta_{kj} A_{kj}^S \delta_{ij}, & \frac{\partial A_{kj}^S}{\partial \vec{v}_i} &= +\Theta_{kj} A_{kj}^C \delta_{ij}. \end{aligned}$$

Using the above equations, the Hessian of the log-posterior distribution  $\nabla^2 \Psi^{\text{CIS}}(\vec{a}, \vec{v})$  is derived for each  $i, j$  as follows:

$$\begin{aligned} (\text{B2}) \quad \frac{\partial^2}{\partial \vec{a}_i \partial \vec{a}_j} \Psi^{\text{CIS}}(\vec{a}, \vec{v}) &= -A_{ki}^C \sigma_k^{-2} A_{kj}^C - A_{ki}^S \sigma_k^{-2} A_{kj}^S \\ &- \delta_{ij} \varepsilon_k^C \sigma_k^{-2} A_{kj}^C - \delta_{ij} \varepsilon_k^S \sigma_k^{-2} A_{kj}^S \\ &- [\Sigma_a^{-1}]_{ij}, \end{aligned} \quad (\text{C3})$$

$$\begin{aligned} \frac{\partial^2}{\partial \vec{v}_i \partial \vec{v}_j} \Psi^{\text{CIS}}(\vec{a}, \vec{v}) &= -\Theta_{ki} A_{ki}^C \sigma_k^{-2} \Theta_{kj} A_{kj}^C - \Theta_{ki} A_{ki}^S \sigma_k^{-2} \Theta_{kj} A_{kj}^S \\ &+ \delta_{ij} \varepsilon_k^C \sigma_k^{-2} \Theta_{kj}^2 A_{kj}^C + \delta_{ij} \varepsilon_k^S \sigma_k^{-2} \Theta_{kj}^2 A_{kj}^S \\ &- [K_v^{-1}]_{ij}, \end{aligned} \quad (\text{C4})$$

$$\begin{aligned} \frac{\partial^2}{\partial \vec{a}_i \partial \vec{v}_j} \Psi^{\text{CIS}}(\vec{a}, \vec{v}) &= +A_{ki}^C \sigma_k^{-2} \Theta_{kj} A_{kj}^S - A_{ki}^S \sigma_k^{-2} \Theta_{kj} A_{kj}^C \\ &+ \delta_{ij} \varepsilon_k^C \sigma_k^{-2} \Theta_{kj} A_{kj}^S - \delta_{ij} \varepsilon_k^S \sigma_k^{-2} \Theta_{kj} A_{kj}^C \\ &= \frac{\partial^2}{\partial \vec{v}_j \partial \vec{a}_i} \Psi^{\text{CIS}}(\vec{a}, \vec{v}), \end{aligned} \quad (\text{C5})$$

where the summation over  $k$  is implied.

<sup>1</sup>Z. Yoshida, S. M. Mahajan, T. Mizushima, Y. Yano, H. Saitoh, and J. Morikawa. Generalized two-fluid equilibria: Understanding RT-1 experiments and beyond. *Physics of Plasmas*, 17(11):112507, 11 2010.

<sup>2</sup>Z. Yoshida, H. Saitoh, Y. Yano, H. Mikami, N. Kasaoka, W. Sakamoto, J. Morikawa, M. Furukawa, and S. M. Mahajan. Self-organized confinement by magnetic dipole: recent results from rt-1 and theoretical modeling. *Plasma Physics and Controlled Fusion*, 55(1):014018, dec 2012.

<sup>3</sup>Zensho YOSHIDA, Yuichi OGAWA, Junji MORIKAWA, Sho WATANABE, Yoshihisa YANO, Shoichi MIZUMAKI, Taizo TOSAKA, Yasumi OHTANI, Atsuro HAYAKAWA, and Masanao SHIBUI. First plasma in the rt-1 device. *Plasma and Fusion Research*, 1:008–008, 2006.

<sup>4</sup>M. Nishiura, Z. Yoshida, H. Saitoh, Y. Yano, Y. Kawazura, T. Nogami, M. Yamasaki, T. Mushiake, and A. Kashyap. Improved beta (local beta > 1) and density in electron cyclotron resonance heating on the rt-1 magnetosphere plasma. *Nuclear Fusion*, 55(5):053019, apr 2015.

- <sup>5</sup>M. Nishiura, Y. Kawazura, Z. Yoshida, N. Kenmochi, Y. Yano, H. Saitoh, M. Yamasaki, T. Mushiake, A. Kashyap, N. Takahashi, M. Nakatsuka, and A. Fukuyama. Ion cyclotron resonance heating system in the RT-1 magnetospheric plasma. *Nuclear Fusion*, 57(8):086038, jul 2017.
- <sup>6</sup>K. Nakamura, M. Nishiura, N. Takahashi, Z. Yoshida, N. Kenmochi, T. Sugata, S. Katsura, and J. Howard. Coherence-imaging spectroscopy for 2D distribution of ion temperature and flow velocity in a laboratory magnetosphere. *Review of Scientific Instruments*, 89(10):10D133, 10 2018.
- <sup>7</sup>Kenji Ueda, Masaki Nishiura, Naoki Kenmochi, Zensho Yoshida, and Kaori Nakamura. Calibration of coherence imaging spectroscopy using spectral line sources. *Review of Scientific Instruments*, 92(7):073501, 07 2021.
- <sup>8</sup>J Howard, C Michael, F Glass, and A Danielsson. Time-resolved two-dimensional plasma spectroscopy using coherence-imaging techniques. *Plasma Physics and Controlled Fusion*, 45(7):1143–1166, may 2003.
- <sup>9</sup>J Howard. Coherence imaging spectro-polarimetry for magnetic fusion diagnostics. *J. Phys. B At. Mol. Opt. Phys.*, 43(14):144010, July 2010.
- <sup>10</sup>John Howard, C. Michael, H. Chen, R. Lester, A. Thorman, and J. Chung. Spectro-polarimetric optical systems for imaging plasma internal fields, structures and flows. *Journal of Instrumentation*, 10(09):P09023–P09023, sep 2015.
- <sup>11</sup>R Lester, Y Zhai, C Corr, and J Howard. Coherence imaging for ion temperature and flow measurements in a low-temperature helicon plasma source. *Plasma Sources Sci. Technol.*, 25(1):015025, February 2016.
- <sup>12</sup>J Howard, A Diallo, M Creese, S L Allen, R M Ellis, W Meyer, M E Fenstermacher, G D Porter, N H Brooks, M E Van Zeeland, and R L Boivin. Coherence imaging of flows in the DIII-D divertor. *Contrib. Plasma Phys.*, 51(2-3):194–200, March 2011.
- <sup>13</sup>S. L. Allen, C. M. Samuelli, W. H. Meyer, and J. Howard. Laser calibration of the DIII-D coherence imaging system. *Review of Scientific Instruments*, 89(10):10E110, 09 2018.
- <sup>14</sup>S A Silburn, J R Harrison, J Howard, K J Gibson, H Meyer, C A Michael, and R M Sharples. Coherence imaging of scrape-off-layer and divertor impurity flows in the mega amp spherical tokamak (invited). *Rev. Sci. Instrum.*, 85(11):11D703, November 2014.
- <sup>15</sup>Dorothea Gradic, Valeria Perseo, Ralf König, and David Ennis. A new calibration implementation for doppler coherence imaging spectroscopy. *Fusion Engineering and Design*, 146:995 – 998, 2019. SI:SOFT-30.
- <sup>16</sup>Valeria Perseo, Dorothea Gradic, Ralf König, Oliver P. Ford, Carsten Killer, Olaf Grulke, David A. Ennis, and W7-X Team. Coherence imaging spectroscopy at Wendelstein 7-X for impurity flow measurements. *Review of Scientific Instruments*, 91(1):013501, 01 2020.
- <sup>17</sup>T Long, J S Allcock, L Nie, R M Sharples, M Xu, R Ke, S Zhang, S A Silburn, J Howard, Y Yu, B Yuan, Z H Wang, X M Song, L Liu, and X R Duan. Doppler coherence imaging of scrape-off-layer impurity flows in the HL-2A tokamak. *Rev. Sci. Instrum.*, 91(8):083504, August 2020.
- <sup>18</sup>J Howard, A Diallo, M Creese, B D Blackwell, S L Allen, R M Ellis, G D Porter, W Meyer, M E Fenstermacher, N H Brooks, M E Van Zeeland, and R L Boivin. Doppler coherence imaging and tomography of flows in tokamak plasmas (invited). *Rev. Sci. Instrum.*, 81(10):10E528, October 2010.
- <sup>19</sup>W. H. Meyer, S. L. Allen, C. M. Samuelli, and M. E. Fenstermacher. Tomographic analysis of tangential viewing cameras (invited). *Review of Scientific Instruments*, 89(10):10K110, 10 2018.
- <sup>20</sup>Bingli Li, Tianbo Wang, Lin Nie, Ting Long, Zijie Liu, Hao Wu, Rui Ke, Zhanhui Wang, Yi Yu, and Min Xu. Tomography of emissivity for doppler coherence imaging spectroscopy diagnostic in HL-2A. *Plasma Sci. Technol.*, 23(9):095104, September 2021.
- <sup>21</sup>Bingli Li, Tianbo Wang, Lin Nie, Ting Long, Xiaoyi Zhang, R M Sharples, Min Xu, Zhanhui Wang, Zhipeng Chen, Hao Wu, Zijie Liu, Rui Ke, Xiaolong Zhang, Shaodong Jiao, Wanjun Qing, Ye Tian, and Yuan Pan. Reconstruction of the emissivity and flow for doppler coherence imaging spectroscopy (CIS) on J-TEXT. *Fusion Eng. Des.*, 184(113271):113271, November 2022.
- <sup>22</sup>Kenji Ueda and Masaki Nishiura. Nonlinear gaussian process tomography with imposed non-negativity constraints on physical quantities for plasma diagnostics (arxiv.2410.11454), 2024.
- <sup>23</sup>Jakob Svensson. Non-parametric tomography using gaussian processes. *JET Internal report*, 2011.
- <sup>24</sup>Dong Li, J. Svensson, H. Thomsen, F. Medina, A. Werner, and R. Wolf. Bayesian soft X-ray tomography using non-stationary Gaussian Processes. *Review of Scientific Instruments*, 84(8):083506, 08 2013.
- <sup>25</sup>T. Wang, D. Mazon, J. Svensson, D. Li, A. Jardin, and G. Verdoolaege. Gaussian process tomography for soft x-ray spectroscopy at WEST without equilibrium information. *Review of Scientific Instruments*, 89(6):063505, 06 2018.
- <sup>26</sup>Mark Gibbs. *Bayesian Gaussian Processes for Regression and Classification*. PhD thesis, University of Cambridge, 1997.
- <sup>27</sup>Carl Edward Rasmussen and Christopher K. I. Williams. *Gaussian Processes for Machine Learning (Adaptive Computation and Machine Learning)*. The MIT Press, 2005.
- <sup>28</sup>M Kuss and C Rasmussen. Assessing approximate inference for binary gaussian process classification. *J. Mach. Learn. Res.*, 6:1679–1704, December 2005.
- <sup>29</sup>D. Gradic, V. Perseo, D.M. Kriete, M. Krychowiak, R. König, Y. Feng, M. Otte, T. Sunn Pedersen, Y. Gao, M. Jakubowski, G. Schlisio, F. Warmer, and the W7-X Team. 2d coherence imaging measurements of c2+ ion temperatures in the divertor of wendelstein 7-x. *Nuclear Fusion*, 61(10):106041, oct 2021.
- <sup>30</sup>David M Kriete, Valeria Perseo, Dorothea Gradic, David A Ennis, Ralf König, David A Maurer, and W7-X Team. Multi-delay coherence imaging spectroscopy optimized for ion temperature measurements in the divertor plasma of the wendelstein 7-X stellarator. *Rev. Sci. Instrum.*, 95(7), July 2024.